Inorg. Chem. **2007**, *46*, 4632–4641

Combined Experimental and Theoretical Study on Aromatic Hydroxylation by Mononuclear Nonheme Iron(IV)–Oxo Complexes

Sam P. de Visser,*,‡ Kyungeun Oh,† Ah-Rim Han,† and Wonwoo Nam*,†

Department of Chemistry, Division of Nano Sciences, and Center for Biomimetic Systems, Ewha Womans University, Seoul 120-750, Korea, and The Manchester Interdisciplinary Biocenter and the School of Chemical Engineering and Analytical Science, The University of Manchester, 131 Princess Street, Manchester M1 7DN, United Kingdom

Received March 9, 2007

The hydroxylation of aromatic compounds by mononuclear nonheme iron(IV)–oxo complexes, $[Fe^{IV}(Bn\text{-}tpen)(O)]^{2+}$ (Bn-tpen = *N*-benzyl-*N*,*N*′,*N*′-tris(2-pyridylmethyl)ethane-1,2-diamine) and $[Fe^{IV}(N4Py)(O)]^{2+}$ (N4Py = *N*,*N*-bis(2-pyridylmethyl)-*N*-bis(2-pyridyl)methylamine), has been investigated by a combined experimental and theoretical approach. In the experimental work, we have performed kinetic studies of the oxidation of anthracene with nonheme iron(IV)–oxo complexes generated in situ, thereby determining kinetic and thermodynamic parameters, a Hammett ρ value, and a kinetic isotope effect (KIE) value. A large negative Hammett ρ value of –3.9 and an inverse KIE value of 0.9 indicate that the iron–oxo group attacks the aromatic ring via an electrophilic pathway. By carrying out isotope labeling experiments, the oxygen in oxygenated products was found to derive from the nonheme iron(IV)–oxo species. In the theoretical work, we have conducted density functional theory (DFT) calculations on the hydroxylation of benzene by $[Fe^{IV}(N4Py)(O)]^{2+}$. The calculations show that the reaction proceeds via two-state reactivity patterns on competing triplet and quintet spin states via an initial rate determining electrophilic substitution step. In analogy to heme iron(IV)–oxo catalysts, the ligand is noninnocent and actively participates in the reaction mechanism by reshuttling a proton from the *ipso* position to the oxo group. Calculated kinetic isotope effects of C_6H_6 versus C_6D_6 confirm an inverse isotope effect for the electrophilic substitution pathway. Based on the experimental and theoretical results, we have concluded that the aromatic ring oxidation by mononuclear nonheme iron(IV)–oxo complexes does not occur via a hydrogen atom abstraction mechanism but involves an initial electrophilic attack on the π-system of the aromatic ring to produce a tetrahedral radical or cationic σ-complex.

Introduction

Oxygen-activating enzymes with mononuclear nonheme iron active sites are involved in many metabolically important oxidative transformations in nature.[1] In the catalytic cycles of dioxygen activation by these enzymes, high-valent iron(IV)−oxo species are frequently invoked as the key intermediates responsible for the oxidation of organic substrates.[1] Very recently, such nonheme iron(IV)−oxo intermediates have been identified in both enzymatic and biomimetic reactions.[2−5] A high-valent iron(IV)−oxo intermediate has been characterized as an active oxidizing species in the catalytic cycle of *Escherichia coli* taurine, namely an α-ketoglutarate-dependent dioxygenase (TauD).[2] In biomimetic studies, mononuclear nonheme iron(IV)−oxo complexes bearing tetradentate N4 and pentadentate N5 and N4S

* To whom correspondence should be addressed. E-mail: wwnam@ewha.ac.kr (W.N.), sam.devisser@manchester.ac.uk (S.P.d.V.).
† Ewha Womans University.
‡ The University of Manchester.

(1) (a) Neidig, M. L.; Solomon, E. I. *Chem. Commun*. **2005**, 5843−5863. (b) Abu-Omar, M. M.; Loaiza, A.; Hontzeas, N. *Chem. Rev*. **2005**, *105*, 2227−2252. (c) Decker, A.; Solomon, E. I. *Curr. Opin. Chem. Biol*. **2005**, *9*, 152−163. (d) Kryatov, S. V.; Rybak-Akimova, E. V.; Schindler, S. *Chem. Rev*. **2005**, *105*, 2175−2226. (e) Borovik, A. S. *Acc. Chem. Res*. **2005**, *38*, 54−61.

(2) (a) Price, J. C.; Barr, E. W.; Tirupati, B.; Bollinger, J. M., Jr.; Krebs, C. *Biochemistry* **2003**, *42*, 7497−7508. (b) Price, J. C.; Barr, E. W.; Glass, T. E.; Krebs, C.; Bollinger, J. M., Jr. *J. Am. Chem. Soc*. **2003**, *125*, 13008−13009. (c) Riggs−Gelasco, P. J.; Price, J. C.; Guyer, R. B.; Brehm, J. H.; Barr, E. W.; Bollinger, J. M., Jr.; Krebs, C. *J. Am. Chem. Soc*. **2004**, *126*, 8108−8109. (d) Bollinger, J. M., Jr.; Price, J. C.; Hoffart, L. M.; Barr, E. W.; Krebs, C. *Eur. J. Inorg. Chem*. **2005**, 4245−4254. (e) Bollinger, J. M., Jr.; Krebs, C. *J. Inorg. Biochem*. **2006**, *100*, 586−605.

(3) (a) Shan, X.; Que, L., Jr. *J. Inorg. Biochem*. **2006**, *100*, 421−433. (b) Decker, A.; Clay, M. D.; Solomon, E. I. *J. Inorg. Biochem*. **2006**, *100*, 697−706. (c) Neese, F. *J. Inorg. Biochem*. **2006**, *100*, 716−726.

10.1021/ic700462h CCC: $37.00
Published on Web 04/20/2007

ligands have been synthesized and characterized with various spectroscopic techniques including X-ray crystallography.[3−5] The synthetic nonheme iron(IV)−oxo complexes have shown reactivities in a variety of oxidation reactions, including alkane hydroxylation, olefin epoxidation, and the oxidation of PPh_3, sulfides, and alcohols.[4,5]

Aromatic hydroxylation is an important chemical process mediated by many metalloenzymes, including cytochromes P450 and nonheme iron mono- and dioxygenases.[6,7] In mononuclear nonheme iron enzymes, aromatic amino acid hydroxylases, such as phenylalanine, tyrosine, and tryptophan hydroxylases, catalyze the aromatic hydroxylation of the namesake amino acids, concomitant with the two-electron oxidation of the requisite organic cofactor tetrahydropterin to its quinonoid dihydropterin form.[8] A mechanism was proposed in which iron(IV)−oxo intermediates are involved as active oxidants in the hydroxylation of aromatic rings, although such iron(IV)−oxo species have not yet been experimentally observed in the catalytic cycles of the enzymes. In biomimetic studies, the catalytic hydroxylation of aromatic compounds by nonheme iron(II) complexes has been demonstrated in a number of cases.[9,10] Notably, Que and co-workers have shown that mononuclear nonheme iron(II) complexes in combination with alkyl hydroperoxides are capable of oxygenating a pendent aromatic ring on the ligand.[9] The authors have provided mechanistic evidence that metal-centered electrophilic oxidants, presumably mononuclear nonheme iron(IV)−oxo intermediates, are involved in the arene hydroxylations, but direct evidence for the participation of such intermediates in the catalytic cycles has yet to be reported. More recently, Rybak-Akimova, Nam, and their co-workers demonstrated independently that intermediates generated in the reactions of mononuclear nonheme iron(II) complexes and oxidants such as H_2O_2 and *m*-chloroperbenzoic acid hydroxylate benzoic acids to the corresponding salicylic acids efficiently.[11,12] However, the nature of active oxidizing intermediates and mechanisms for the aromatic ring hydroxylations were not clearly understood in the studies. Therefore, we deemed it timely to do a combined experimental and theoretical study into the mechanisms of aromatic hydroxylation by nonheme iron−oxo biomimetics. Since the aromatic hydroxylation reactions reported so far have been investigated mainly under catalytic conditions, we have performed mechanistic studies of the aromatic ring hydroxylation with in situ-generated mononuclear nonheme iron(IV)−oxo complexes. To support the experimentally obtained conclusions we conducted density functional theory (DFT) calculations on the hydroxylation of benzene by a nonheme iron(IV)−oxo intermediate for the first time. These experimental and theoretical results have been discussed in the light of elucidating mechanisms of the aromatic ring hydroxylation by mononuclear nonheme iron(IV)−oxo complexes.

Results and Discussion

Reactivities of Nonheme Iron(IV)−Oxo Complexes in Aromatic Hydroxylation. The mononuclear nonheme iron(IV)−oxo complexes, $[Fe^{IV}(Bn\text{-}tpen)(O)]^{2+}$ (**1**) (Bn-tpen = *N*-benzyl-*N*,*N*′,*N*′-tris(2-pyridylmethyl)ethane-1,2-diamine) and $[Fe^{IV}(N4Py)(O)]^{2+}$ (**2**) (N4Py = *N*,*N*-bis(2-pyridylmethyl)-*N*-bis(2-pyridyl)methylamine), used in this work are shown in Figure 1.[4c] The reactive species were prepared by treating their corresponding iron(II) complexes, Fe(Bn-tpen)$(CF_3SO_3)_2$ and Fe(N4Py)$(CF_3SO_3)_2$, with solid iodosylbenzene (PhIO) in a solvent mixture of CH_3CN and CH_2Cl_2 (1:1) at 25 °C. Upon addition of anthracene to the solutions,[13] the intermediates reverted to the starting iron(II) complexes with a clear isosbestic point at 490 nm for **1** and 538 nm for **2** and showed pseudo-first-order decay as monitored by a

(4) (a) Rohde, J.-U.; In, J.-H.; Lim, M. H.; Brennessel, W. W.; Bukowski, M. R.; Stubna, A.; Münck, E.; Nam, W.; Que, L., Jr. *Science* **2003**, *299*, 1037−1039. (b) Lim, M. H.; Rohde, J.-U.; Stubna, A.; Bukowski, M. R.; Costas, M.; Ho, R. Y. N.; Münck, E.; Nam, W.; Que, L., Jr. *Proc. Natl. Acad. Sci. U.S.A.* **2003**, *100*, 3665−3670. (c) Kaizer, J.; Klinker, E. J.; Oh, N. Y.; Rohde, J.-U.; Song, W. J.; Stubna, A.; Kim, J.; Münck, E.; Nam, W.; Que, L., Jr. *J. Am. Chem. Soc.* **2004**, *126*, 472−473. (d) Kim, S. O.; Sastri, C. V.; Seo, M. S.; Kim, J.; Nam, W. *J. Am. Chem. Soc.* **2005**, *127*, 4178−4179. (e) Oh, N. Y.; Suh, Y.; Park, M. J.; Seo, M. S.; Kim, J.; Nam, W. *Angew. Chem., Int. Ed.* **2005**, *44*, 4235−4239. (f) Sastri, C. V.; Park, M. J.; Ohta, T.; Jackson, T. A.; Stubna, A.; Seo, M. S.; Lee, J.; Kim, J.; Kitagawa, T.; Münck, E.; Que, L., Jr.; Nam, W. *J. Am. Chem. Soc.* **2005**, *127*, 12494−12495. (g) Bukowski, M. R.; Koehntop, K. D.; Stubna, A.; Bominaar, E. L.; Halfen, J. A.; Münck, E.; Nam, W.; Que, L., Jr. *Science* **2005**, *310*, 1000−1002. (h) Klinker, E. J.; Kaizer, J.; Brennessel, W. W.; Woodrum, N. L.; Cramer, C. J.; Que, L., Jr. *Angew. Chem., Int. Ed.* **2005**, *44*, 3690−3694. (i) Sastri, C. V.; Oh, K.; Lee, Y. J.; Seo, M. S.; Shin, W.; Nam, W. *Angew. Chem., Int. Ed.* **2006**, *45*, 3992−3995. (j) Park, M. J.; Lee, J.; Suh, Y.; Kim, J.; Nam, W. *J. Am. Chem. Soc.* **2006**, *128*, 2630−2634.

(5) (a) Grapperhaus, C. A.; Mienert, B.; Bill, E.; Weyhermüller, T.; Wieghardt, K. *Inorg. Chem.* **2000**, *39*, 5306−5317. (b) Balland, V.; Charlot, M.-F.; Banse, F.; Girerd, J.-J.; Mattioli, T. A.; Bill, E.; Bartoli, J.-F.; Battioni, P.; Mansuy, D. *Eur. J. Inorg. Chem.* **2004**, 301−308. (c) Martinho, M.; Banse, F.; Bartoli, J.-F.; Mattioli, T. A.; Battioni, P.; Horner, O.; Bourcier, S.; Girerd, J.-J. *Inorg. Chem.* **2005**, *44*, 9592−9596.

(6) (a) Sono, M.; Roach, M. P.; Coulter, E. D.; Dawson, J. H. *Chem. Rev.* **1996**, *96*, 2841−2887. (b) Meunier, B. In *Biomimetic Oxidations Catalyzed by Transition Metal Complexes*; Meunier, B., Ed.; Imperial College Press: London, 2000; pp 171−214. (c) Meunier, B.; de Visser, S. P.; Shaik, S. *Chem. Rev.* **2004**, *104*, 3947−3980. (d) *Cytochrome P450: Structure, Mechanism, and Biochemistry*, 3rd ed.; Ortiz de Montellano, P. R., Ed.; Kluwer Academic/Plenum Publishers: New York, 2005. (e) Shaik, S.; Kumar, D.; de Visser, S. P.; Altun, A.; Thiel, W. *Chem. Rev.* **2005**, *105*, 2279−2328.

(7) (a) Solomon, E. I.; Brunold, T. C.; Davis, M. I.; Kemsley, J. N.; Lee, S.-K.; Lehnert, N.; Neese, F.; Skulan, A. J.; Yang, Y.-S.; Zhou, J. *Chem. Rev.* **2000**, *100*, 235−349. (b) Costas, M.; Mehn, M. P.; Jensen, M. P.; Que, L., Jr. *Chem. Rev.* **2004**, *104*, 939−986.

(8) (a) Flatmark, T.; Stevens, R. C. *Chem. Rev.* **1999**, *99*, 2137−2160. (b) Klinman, J. P. *J. Biol. Inorg. Chem.* **2001**, *6*, 1−13. (c) Fitzpatrick, P. F. *Biochemistry* **2003**, *42*, 14083−14091.

(9) (a) Lange, S. J.; Miyake, H.; Que, L., Jr. *J. Am. Chem. Soc.* **1999**, *121*, 6330−6331. (b) Jensen, M. P.; Lange, S. J.; Mehn, M. P.; Que, E. L.; Que, L., Jr. *J. Am. Chem. Soc.* **2003**, *125*, 2113−2128.

(10) (a) Kitajima, N.; Ito, M.; Fukui, H.; Moro−oka, Y. *J. Am. Chem. Soc.* **1993**, *115*, 9335−9336. (b) Funabiki, T.; Yokomizo, T.; Suzuki, S.; Yoshida, S. *Chem. Commun.* **1997**, 151−152. (c) Menage, S.; Galey, J.-B.; Dumats, J.; Hussler, G.; Seite, M.; Luneau, I. G.; Chottard, G.; Fontecave, M. *J. Am. Chem. Soc.* **1998**, *120*, 13370−13382. (d) Mekmouche, Y.; Menage, S.; Toia-Duboc, C.; Fontecave, M.; Galey, J.-B.; Lebrun, C.; Pecaut, J. *Angew. Chem., Int. Ed.* **2001**, *40*, 949−952. (e) Mehn, M. P.; Fujisawa, K.; Hegg, E. L.; Que, L., Jr. *J. Am. Chem. Soc.* **2003**, *125*, 7828−7842. (f) Avenier, F.; Dubois, L.; Latour, J.-M. *New. J. Chem.* **2004**, *28*, 782−784.

(11) Taktak, S.; Flook, M.; Foxman, B. M.; Que, L., Jr.; Rybak-Akimova, E. V. *Chem. Commun.* **2005**, 5301−5303.

(12) Oh, N. Y.; Seo, M. S.; Lim, M. H.; Consugar, M. B.; Park, M. J.; Rohde, J.-U.; Han, J.; Kim, K. M.; Kim, J.; Que, L., Jr.; Nam, W. *Chem. Commun.* **2005**, 5644−5646.

(13) The intermediates, **1** and **2**, do not react with benzene and naphthalene due to the low reactivity of the nonheme iron(IV)−oxo species.

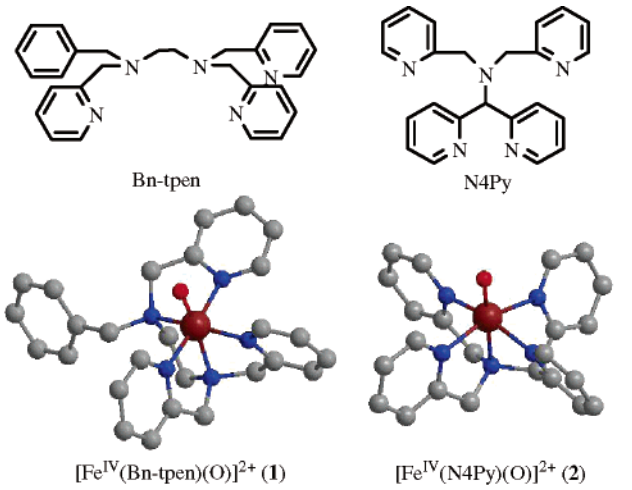

Figure 1. Structure of ligands and iron(IV)−oxo complexes used in this study. The hydrogen atoms have been omitted for clarity.

UV−vis spectrophotometer (Figure 2a for **1** and Supporting Information, Figure S1 for **2**). Pseudo-first-order fitting of the kinetic data allowed us to determine the k_{obs} values to be $5.9(4)\bullet10^{-2}$ s^{-1} and $2.5(3)\bullet10^{-3}$ s^{-1} for the reactions of **1** and **2** at 25 °C (Figure 2a and Figure S1, insets), indicating that **1** is more reactive than **2** toward aromatic hydroxylation. The greater reactivity of **1** than **2** has also been observed in alkane hydroxylations.[4c] Product analysis of the reaction mixtures revealed that anthraquinone was produced in high yields in the reactions (~40% based on intermediates generated). The formation of quinone products has been well documented in aromatic hydroxylation reactions catalyzed by metalloporphyrins,[14−16] and a mechanism has been proposed in which two metal−oxo complexes are needed for the formation of one quinone product.[14,15] The pseudo-first-order rate constants increased proportionally with substrate concentration, thus leading us to determine the second-order rate constant to be $6.8(5)\bullet10^{-1}$ $M^{-1}\bullet s^{-1}$ in the anthracene oxidation by **1** (Figure 2b). Activation parameters for the anthracene oxidation were determined by plotting first-order rate constants measured at different temperatures (273−298 K) against $1/T$ (Figure 2c); the activation enthalpy and entropy values were calculated to be $\Delta H^{\ddagger} = 13(1)$ kcal•mol^{-1} and $\Delta S^{\ddagger} = -22(2)$ cal•mol^{-1}•K^{-1}.

We then investigated the electronic effect of substrate on the aromatic hydroxylation by nonheme iron(IV)−oxo species. The first-order rate constants determined in the oxidation of various *para*-X-substituted anthracenes by **1** indicate that the electron-donating ability of the *para*-substituents influences the reaction rate significantly (Supporting Information, Table S1). By plotting the rates as a function of σ_p of the *para*-substituents, a good linear correlation was obtained with a large negative Hammett ρ value of −3.9(2) (Figure 3), indicating a high charge separation in the transition state of the aromatic ring oxidation. Such a large negative ρ value implies that the iron−oxo group attacks the aromatic ring

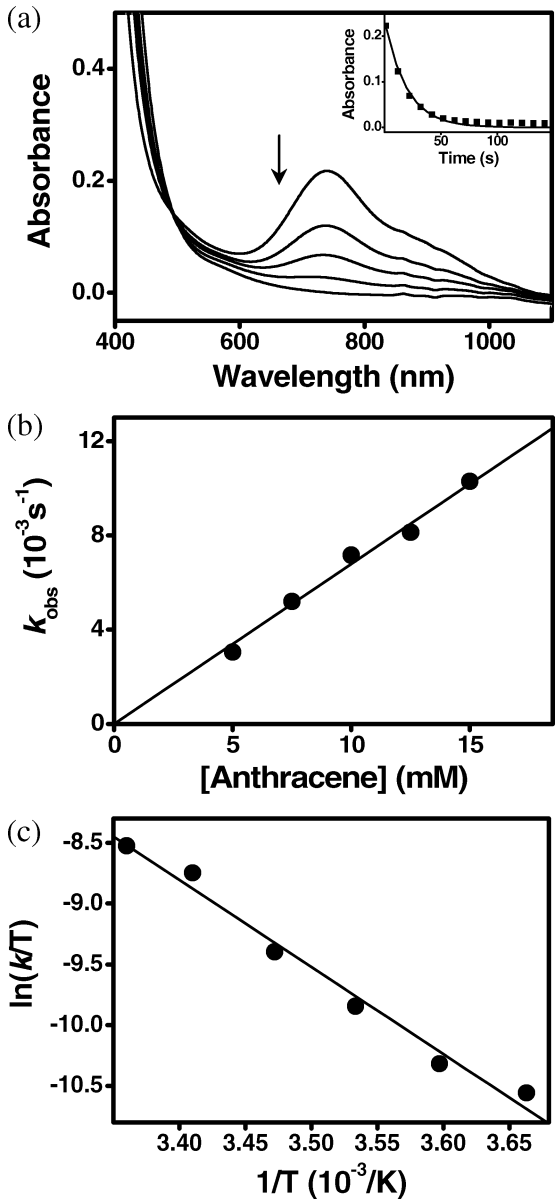

Figure 2. (a) UV−vis spectral changes of **1** (1 mM) upon addition of 10 equiv of anthracene (10 mM) at 25 °C. Inset shows absorbance traces monitored at 737 nm. (b) Plot of k_{obs} against anthracene concentration to determine the second-order rate constant at 0 °C. (c) Plot of first-order-rate constants against $1/T$ to determine activation parameters.

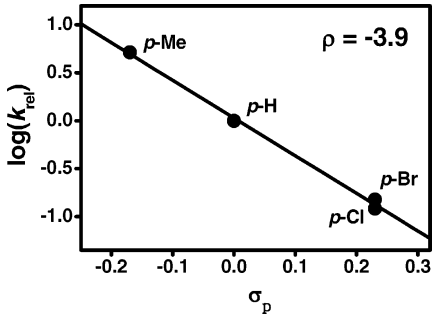

Figure 3. Hammett plot of log k_{rel} against σ_p of *para*-X-substituted anthracenes. First-order rate constants for *para*-substituted anthracenes were determined at 0 °C (Supporting Information, Table S1), and the k_{rel} values were calculated by dividing k_{obs} of *para*-X-anthracene by k_{obs} of anthracene.

(14) (a) Song, R.; Sorokin, A.; Bernadou, J.; Meunier, B. *J. Org. Chem.* **1997**, *62*, 673−678. (b) Sorokin, A.; Meunier, B. *Eur. J. Inorg. Chem.* **1998**, 1269−1281.
(15) Higuchi, T.; Satake, C.; Hirobe, M. *J. Am. Chem. Soc.* **1995**, *117*, 8879−8880.
(16) Khavasi, H. R.; Davarani, S. S. H.; Safari, N. *J. Mol. Catal. A: Chem.* **2002**, *188*, 115−122.

Table 1. Rates Determined in the Hydroxylation of Anthracene and Anthracene-d_{10} by **1** and **2**[a,b]

1			**2**		
rate constant (10^{-3} s^{-1})			rate constant (10^{-3} s^{-1})		
$C_{14}H_{10}$	$C_{14}D_{10}$	k_H/k_D	$C_{14}H_{10}$	$C_{14}D_{10}$	k_H/k_D
7.1	7.7	0.92	2.4	2.8	0.88

[a] Rates were determined by adding 10 equiv of anthracene (10 mM) to a reaction containing **1** or **2** (1 mM each) in a solvent mixture of CH_3CN and CH_2Cl_2 (1:1) at 0 °C for **1** or at 25 °C for **2**. [b] Rate constants are averaged by three determinations.

via an electrophilic pathway. Moreover, it is worth noting that a very small Hammett ρ value was observed in the oxidation of alcohols by nonheme iron(IV)−oxo complexes (i.e., ρ value of ~ -0.1), in which the alcohol oxidation occurs via a hydrogen atom abstraction mechanism.[4e]

Kinetic isotope effects (KIE) were also investigated kinetically in the hydroxylation of undeuterated and deuterated anthracenes by nonheme iron(IV)−oxo complexes (Table 1). The calculated k_H/k_D values of ∼0.9 in the reactions of **1** and **2** indicate the inverse KIE in the aromatic ring oxidation reactions; the observation of the inverse KIE is consistent with the sp^2-to-sp^3 hybridization change during the addition of an electrophilic iron−oxo group to the sp^2 center of aromatic ring to form a σ adduct.[17−19] Further, the KIE value of ∼0.9 rules out a hydrogen atom abstraction mechanism; the oxidation of ethylbenzene and benzyl alcohol by **2** occurs via a hydrogen atom abstraction mechanism, and large KIE values of ∼50 were observed in these reactions.[4c,4e]

Finally, the source of oxygen incorporated into oxygenated products was investigated by carrying out isotope labeling studies in the hydroxylation of anthracene by $[Fe^{IV}(Bn\text{-}tpen)(^{18}O)]^{2+}$ (**1**-^{18}O). First, **1**-^{18}O was prepared by reacting Fe(Bn-tpen)$(OTf)_2$ with PhI^{18}O, and the ^{18}O percentage in **1**-^{18}O was determined to be 75% by taking an Electrospray Ionization Mass Spectrum of the intermediate (Supporting Information, Figure S2).[20] Then, **1**-^{18}O was reacted with anthracene. To increase the accuracy of product analysis, a catalytic hydroxylation of anthracene by $[Fe^{II}(Bn\text{-}tpen)]^{2+}$ and PhIO was also carried out in the presence of $H_2{}^{18}O$ at 25 °C under inert atmosphere. By analyzing the reaction solutions with GC and GC−MS, we found that anthraquinone was produced as a major product (35% based on PhIO added) and that the percentages of M, M + 2, and M + 4 products were 13(3), 36(4), and 51(5)%, respectively (Scheme 1).[21] The observation that the anthraquinone product contained significant amounts of ^{18}O derived from the iron−oxo group demonstrates unambiguously that the source of oxygen incorporated into the product is the iron(IV)−oxo complex.[21] In control experiments, we checked that the oxygen of anthraquinone does not exchange with $H_2{}^{18}O$ under the reaction conditions.

Scheme 1. Incorporation of Isotopically Labeled ^{18}O into Product

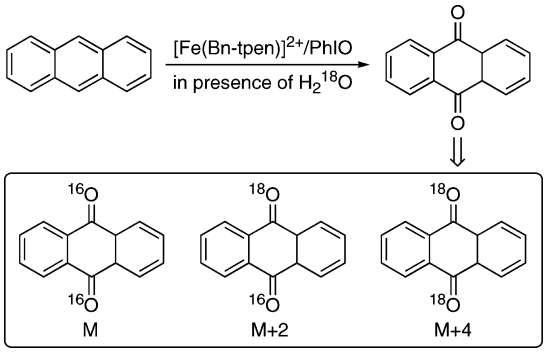

Scheme 2. Possible Reaction Mechanisms of Anthracene Hydroxylation by Nonheme Iron(IV)−Oxo Intermediates

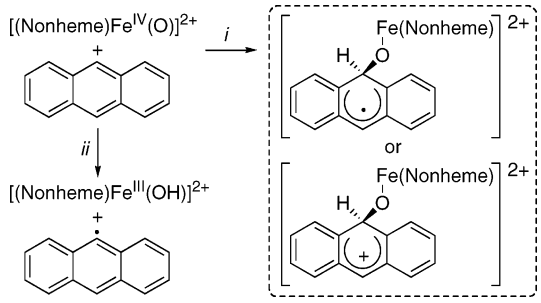

In summary, we have shown that nonheme iron(IV)−oxo complexes are capable of conducting aromatic hydroxylation reactions; the kinetic and thermodynamic parameters were determined in the oxidation of anthracene. Based on the large negative Hammett ρ value and inverse KIE value, we have proposed that the aromatic oxidation does not occur via a hydrogen atom abstraction mechanism (Scheme 2, pathway *ii*) but involves an initial electrophilic attack on the π-system of the aromatic ring to produce a tetrahedral radical or cationic σ-complex (Scheme 2, pathway *i*). By carrying out ^{18}O-labeled water experiments, the oxygen in oxygenated product was found to derive from iron−oxo intermediates.

DFT Calculations on the Hydroxylation of Benzene by Mononuclear Nonheme Iron(IV)−Oxo Species. To support the experimental findings we have performed DFT calculations on a model reaction of aromatic hydroxylation by $[Fe^{IV}(N4Py)(O)]^{2+}$ (**2**) using benzene as a substrate. Earlier DFT calculations[22] showed that **2** reacts with alkanes via two-state reactivity patterns on competing triplet and quintet spin-state surfaces; therefore, here we also calculated the reaction mechanisms on these two spin-state surfaces. The two spin states only differ in the occupation of the metal 3d set of orbitals and ^{3}**2** has occupation $\pi^{*2}_{x^2-y^2}\ \pi^{*1}_{xz}\ \pi^{*1}_{yz}$, while ^{5}**2**

(17) (a) Griffin, G. W.; Horn, K. A. *J. Am. Chem. Soc.* **1987**, *109*, 4919−4926. (b) Hanzlik, R. P.; Ling, K.-H. J. *J. Am. Chem. Soc.* **1993**, *115*, 9363−9370. (c) Vannelli, T.; Hooper, A. B. *Biochemistry* **1995**, *34*, 11743−11749.
(18) Shiota, Y.; Suzuki, K.; Yoshizawa, K. *Organometallics* **2005**, *24*, 3532−3538.
(19) de Visser, S. P.; Shaik, S. *J. Am. Chem. Soc.* **2003**, *125*, 7413−7424.
(20) Seo, M. S.; In, J.-H.; Kim, S. O.; Oh, N. Y.; Hong, J.; Kim, J.; Que, L., Jr.; Nam, W. *Angew. Chem., Int. Ed.* **2004**, *43*, 2417−2420.
(21) (a) Nam, W.; Valentine, J. S. *J. Am. Chem. Soc.* **1993**, *115*, 1772−1778. (b) Bernadou, J.; Fabiano, A.-S.; Robert, A.; Meunier, B. *J. Am. Chem. Soc.* **1994**, *116*, 9375−9376. (c) Lee, K. A.; Nam, W. *J. Am. Chem. Soc.* **1997**, *119*, 1916−1922. (d) Groves, J. T.; Lee, J.; Marla, S. S. *J. Am. Chem. Soc.* **1997**, *119*, 6269−6273. (e) Bernadou, J.; Meunier, B. *Chem. Commun.* **1998**, 2167−2173. (f) Meunier, B.; Bernadou, J. *Struct. Bonding* **2000**, *97*, 1−35.
(22) (a) Kumar, D.; Hirao, H.; Que, L., Jr.; Shaik, S. *J. Am. Chem. Soc.* **2005**, *127*, 8026−8027. (b) Hirao, H.; Kumar, D.; Que, L., Jr.; Shaik, S. *J. Am. Chem. Soc.* **2006**, *128*, 8590−8606.

Scheme 3. Reaction Mechanism and Nomenclature of Structures of Intermediates and Transition States for the Benzene Hydroxylation Reaction by $Fe{=}O(N4Py)^{2+}$ [a]

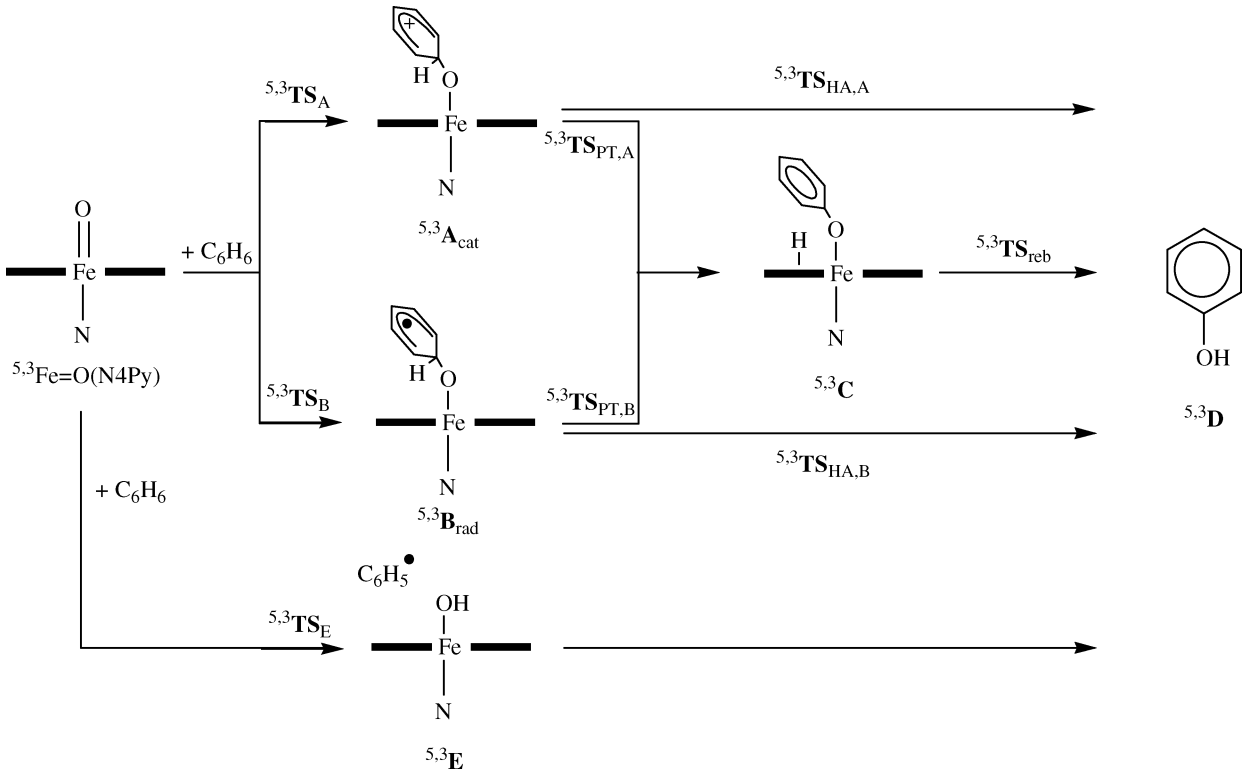

[a] We also calculated a long-range complex (^{5,3}**RC**) between $^{5,3}Fe{=}O(N4Py)^{2+}$ and benzene (not shown in this scheme).

has occupation $\pi^{*1}_{x^2-y^2}$ π^{*1}_{xz} π^{*1}_{yz} σ^{*1}_{xy}.[22] The triplet spin state is the ground state with the quintet spin state higher in energy by 13.1 (LACVP) and 8.0 (LACV3P+*) kcal mol^{-1}, while zero-point corrections at the LACVP level reduce the triplet−quintet energy gap further to 11.9 and 6.7 kcal mol^{-1}, respectively, for the two basis sets. Therefore, the triplet−quintet energy gap is sensitive to the quality of the basis set and ZPE corrections, as observed before by Shaik and coworkers who found the same trends in the energetics.[22] By contrast, other nonheme iron(IV)−oxo species such as the active species of TauD has a quintet spin ground state well separated from the triplet.[23] Therefore, the nature of the ligands bound to iron regulates the triplet−quintet energy splitting and consequently the reactivity patterns. Our optimized geometries of ^{3,5}**2** are shown in Figure S7 of the Supporting Information, and the results are in perfect agreement with earlier work.[22,24]

Subsequently, we calculated the benzene hydroxylation by ^{5,3}**2** using several possible reaction mechanisms (Scheme 3). The top two mechanisms in Scheme 3 are analogous to the ones studied for oxoiron heme catalysts[19,25] and proceed via an electrophilic substitution of benzene with attack on the oxygen atom of the oxoiron group, resulting in the formation of an intermediate species with a cation on the benzene restgroup (^{5,3}**A**) or a radical on the benzene restgroup (^{5,3}**B**). In the case of benzene and ethylbenzene hydroxylation by oxoiron heme models, the mechanisms passing the cationic and radical intermediates were close-lying, and the ordering of the rate determining steps was dependent on small external perturbations such as a dielectric constant or hydrogen bonding.[19,25b] We tested two different mechanisms for the relay of the *ipso* proton to the oxygen atom. First, a direct hydrogen atom (HA) transfer from the *ipso* position of ^{5,3}**A** and ^{5,3}**B** to the oxygen atom to give phenol products via barriers ^{5,3}**TS**$_{HA,A}$ or ^{5,3}**TS**$_{HA,B}$, respectively, was tested. Second, a proton shuttle mechanism via one of the nitrogen atoms of N4Py was tested, whereby first a proton-transfer intermediate (^{5,3}**C**) is formed from ^{5,3}**A** and ^{5,3}**B** via barriers ^{5,3}**TS**$_{PT,A}$ and ^{5,3}**TS**$_{PT,B}$, respectively. Subsequently, the proton is reshuttled to the oxygen atom via a barrier ^{5,3}**TS**$_{reb}$ to finally give the phenol products (^{5,3}**D**). In the case of benzene hydroxylation by oxoiron heme catalysts, the latter mechanism was found to be much lower in energy than a direct hydrogen atom transfer.[19] In addition, we tested a direct hydrogen abstraction from benzene by $Fe{=}O(N4Py)^{2+}$ reactant (^{5,3}**2**) leading to a hydroxoiron complex (^{5,3}**E**) with a nearby benzyl radical, followed by OH rebound to the benzyl radical to form phenol. Alkane hydroxylations by oxoiron heme and nonheme catalysts typically react via an initial hydrogen abstraction followed by rebound of the hydroxo group.[4c,24b,26]

(23) (a) de Visser, S. P. *Angew. Chem., Int. Ed.* **2006**, *45*, 1790−1793. (b) de Visser, S. P. *J. Am. Chem. Soc.* **2006**, *128*, 9813−9824.
(24) (a) de Visser, S. P.; Shaik, S.; Sharma, P. K.; Kumar, D.; Thiel, W. *J. Am. Chem. Soc.* **2003**, *125*, 15779−15788. (b) de Visser, S. P.; Kumar, D.; Cohen, S.; Shacham, R.; Shaik, S. *J. Am. Chem. Soc.* **2004**, *126*, 8362−8363.
(25) (a) Bathelt, C. M.; Ridder, L.; Mulholland, A. J.; Harvey, J. N. *Org. Biomol. Chem.* **2004**, *2*, 2998−3005. (b) de Visser, S. P. *Chem. Eur. J.* **2006**, *12*, 8168−8177.
(26) (a) de Visser, S. P.; Ogliaro, F.; Sharma, P. K.; Shaik, S. *Angew. Chem., Int. Ed.* **2002**, *41*, 1947−1951. (b) de Visser, S. P.; Ogliaro, F.; Sharma, P. K.; Shaik, S. *J. Am. Chem. Soc.* **2002**, *124*, 11809−11826.

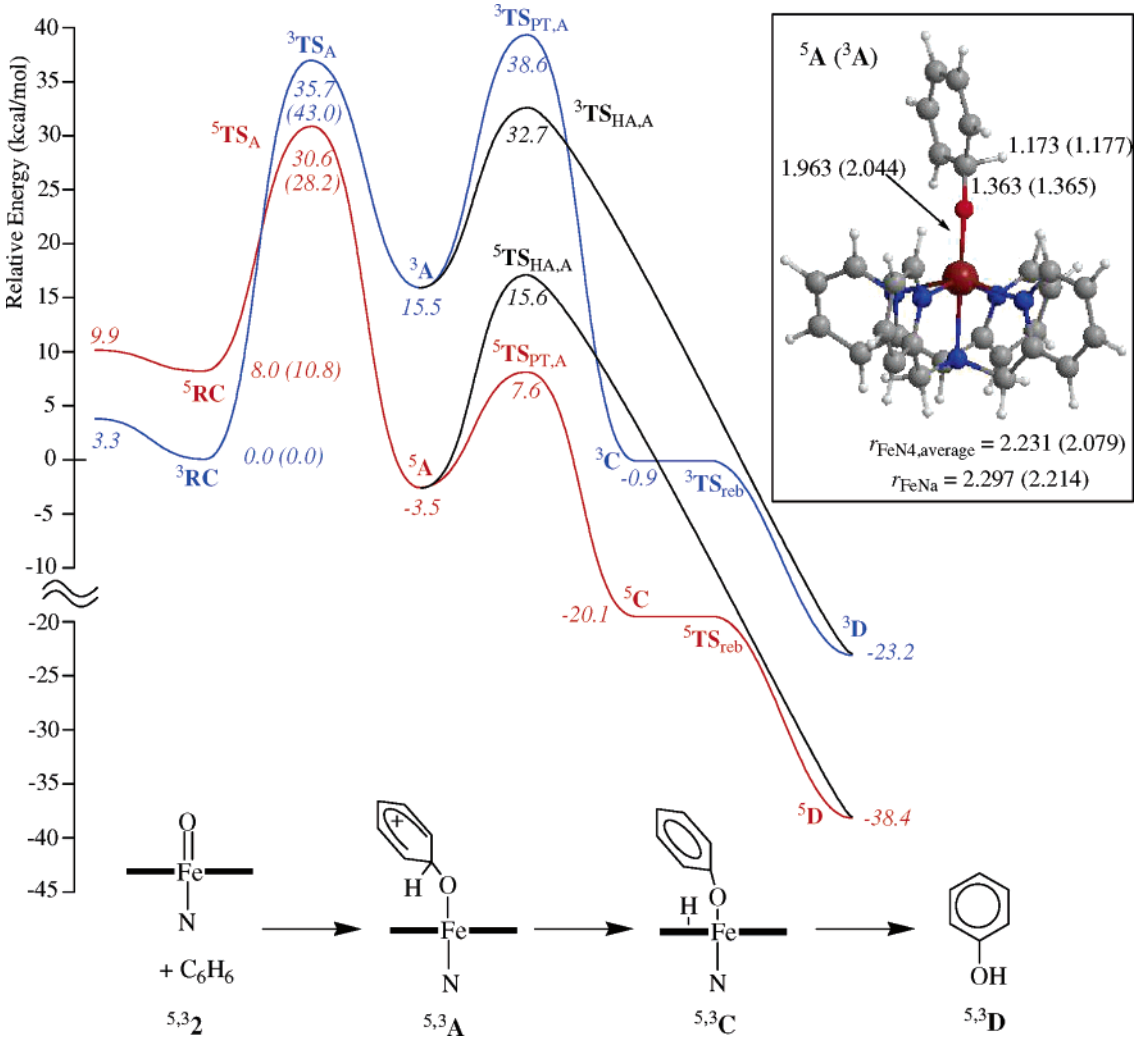

Figure 4. Potential energy surface for the hydroxylation of benzene by ^{5,3}Fe═O(N4Py)$^{2+}$ via cationic intermediates. The proton shuttle mechanism in the triplet spin state is in blue, and the one in the quintet spin state is in red. All energies are obtained at the UB3LYP/LACV3P+* level with ZPE corrections at UB3LYP/LACVP. Energies are in kcal mol^{-1} relative to the reactant complex in the triplet spin state. Values in parentheses are ΔE+ZPE energies with solvent corrections. Also shown are optimized geometries of ^{5,3}**A** with bond distances in Å.

Optimized geometries of all optimized structures are shown in the Supporting Information, while we will focus here on the major trends and reaction mechanisms.

Figure 4 shows the potential energy surface for the reaction mechanisms of benzene hydroxylation via cationic intermediates (^{5,3}**A**), whereas Figure 5 shows the one that passes radical intermediates (^{5,3}**B**). Thus, initially the reaction bifurcates into radical and cationic intermediates (^{5,3}**A**,^{5,3}**B**), but later the surfaces converge again to form structures ^{5,3}**C** and ^{5,3}**D**. The cationic mechanisms require a relatively high C−O formation barrier (^{5,3}**TS**$_A$) of 30.6 (quintet) and 35.7 (triplet) kcal mol^{-1}, while the barriers leading to radical intermediates are significantly lower. In particular, the barrier (^{5}**TS**$_B$) leading to ^{5}**B** is barely higher in energy than the reactant complex and even lower in energy than isolated reactants. This implies that the approach of benzene to ^{5}**2** will rapidly lead to the formation of a radical intermediate without much activation barrier. This contrasts the energetics calculated for benzene hydroxylation by Fe═O(Por)SH, whereby comparable barriers leading to radical and cationic intermediates of around 18 kcal mol^{-1} were obtained.[19] Although the barrier leading to ^{5}**B** is the lowest, we expect fast equilibration between ^{5}**A** and ^{5}**B** as the cationic intermediates (^{5,3}**A**) are substantially lower in energy than the radical intermediates (^{5,3}**B**) by 5.4 (triplet) and 6.9 (quintet) kcal mol^{-1}. The reason for the fact that the cationic intermediates are more stable than the radical ones is because the Fe═O(N4Py) model has an overall charge of +2, and the charge repulsion within the model will favor the cationic intermediates. By contrast, the arene hydroxylation by heme models used an overall neutral system. There are some critical geometric differences between ^{5}**A** and ^{5}**B**, which may have an impact on the triplet−quintet spin-state crossing. Due to double occupation of the $\pi^*_{x^2-y^2}$ orbital in ^{5}**A**, the average Fe−N distance of the four Fe−N bonds in the *xy*-plane of symmetry is considerably longer in ^{5}**A** than in ^{5}**B** (i.e., 2.231 Å versus 2.175 Å), while the axial Fe−N$_a$ distance is virtually the same (compare the structures in Figures 4 and 5). Since the metal is in oxidation state Fe^{II} in ^{5,3}**A** but in Fe^{III} in ^{5,3}**B**, the iron−oxygen bond is longer in **A** (i.e., 1.963 Å in ^{5}**A** and 1.792 Å in ^{5}**B**). Note as well the short C−O distance in ^{5}**A** as compared to ^{5}**B** (i.e., 1.363 Å versus

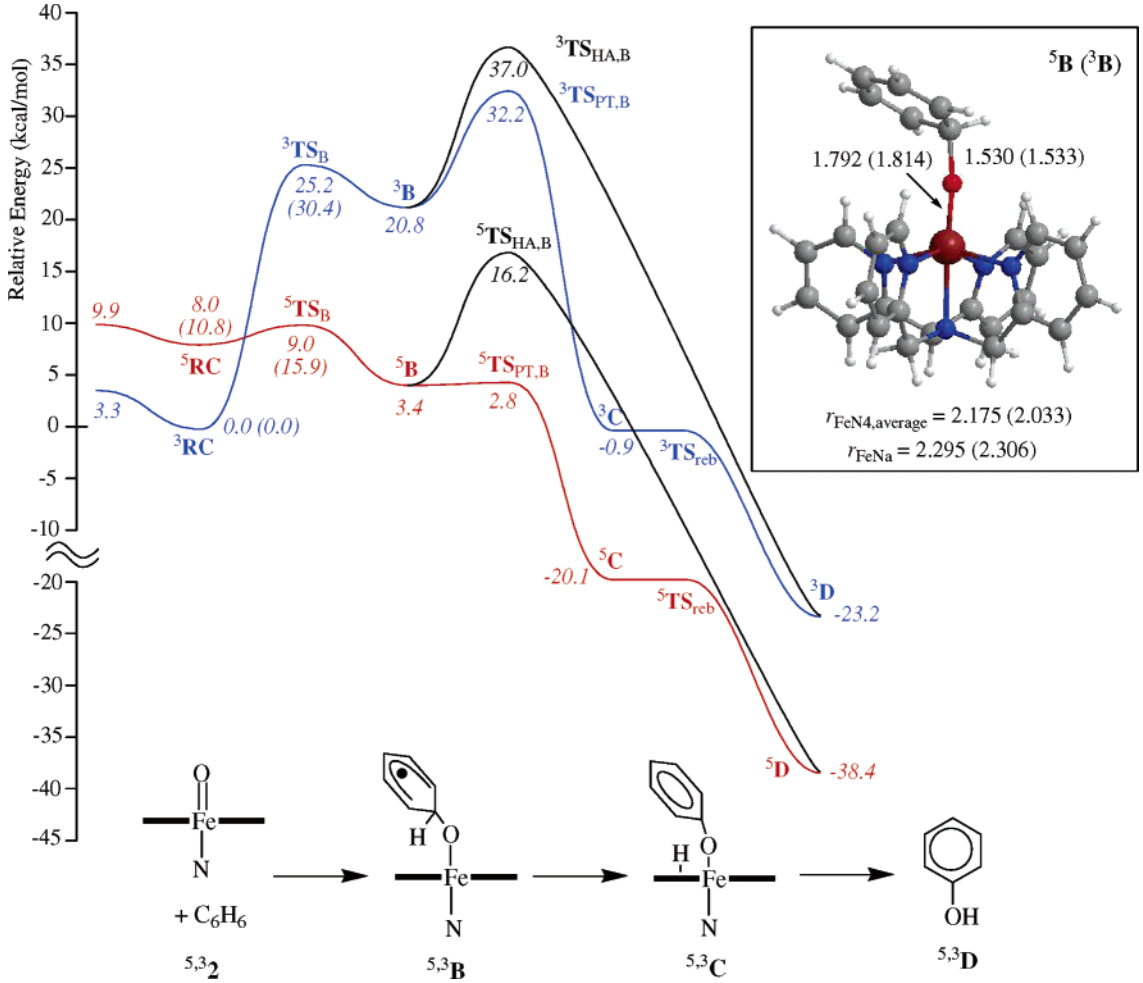

Figure 5. Potential energy surface for the hydroxylation of benzene by ^{5,3}Fe═O(N4Py)$^{2+}$ via radical intermediates. The proton shuttle mechanism in the triplet spin state is in blue, and the one in the quintet spin state is in red. All energies are obtained at the UB3LYP/LACV3P+* level with ZPE corrections at UB3LYP/LACVP. Energies are in kcal mol^{-1} relative to the reactant complex in the triplet spin state. Values in parentheses are ΔE+ZPE energies with solvent corrections. Also shown are optimized geometries of ^{5,3}**B** with bond lengths in Å.

1.530 Å), which is almost a double bond in **A** but a single bond in **B**. Another structural difference between ^{5,3}**A** and ^{5,3}**B** is the fact that the arene group is aligned with the Fe−O bond in the cationic intermediates, whereas it is tilted in the radical intermediates. Although the triplet spin state is the ground state in the reactants, the quintet spin-state surface crosses the triplet spin state before the first transition state, and in the rest of the reaction mechanism the quintet spin state stays the ground state. Thus, since the barriers on the quintet spin-state surface are well lower than those on the triplet spin-state surface, this implies that the population of the quintet spin state in the reactants and the spin-state crossing from the triplet to the quintet spin-state surface during the reaction determine the speed of the reaction and the amount of products formed.

From the intermediate complexes a direct proton shuttle to one of the nitrogen atoms of the N4Py unit can take place to form structure ^{5,3}**C** which thereafter leads to the phenol product ^{5,3}**D** via a negligible barrier. Figure 6 shows the optimized geometries of ^{5,3}**C** and ^{5,3}**D**. Essentially, ^{5,3}**C** has a phenolate anion bound to iron, and the N4Py ligand has undergone a dramatic change, namely one of the pyrimidine rings has lost its Fe−N bond to make space for the incoming proton. Geometrically, the proton is at a similar distance to the oxygen atom as to the C_1 carbon atom: the O−H distance in ^{5,3}**C** is of the same order of magnitude as the C−H distance, so that in principle the proton can be reshuttled to either the oxygen to form product or back to the C_1 carbon atom to either intermediate ^{5,3}**A** or ^{5,3}**B**. However, structure ^{5,3}**C** is well lower in energy than ^{5,3}**A** (by at least 16.3 kcal mol^{-1}) and ^{5,3}**B** (by at least 21.7 kcal mol^{-1}), whereas the formation of product is exothermic. Since, the charge on the oxygen atom is much more negative than the one on the carbon atom, the process leading to product formation will be favorable. Moreover, structures **A** and **B** have less aromaticity in the benzene group than **C**. Reshuttling the proton to the oxygen atom reinstates the broken Fe−N bond to its original geometry. As follows from the geometry scans in Figure S5, the proton reshuttle barriers (^{5,3}**TS**$_{reb}$) on the triplet and quintet spin-state surfaces are negligible, which would imply that ^{5,3}**C** are first-order saddle points; however, frequency calculations confirm them as stable intermediates. Since the reshuttle barrier (^{5,3}**TS**$_{reb}$) is small, the lifetime of ^{5,3}**C** will be limited, and it will be converted into ^{5,3}**D** very quickly. Generally, in the electrophilic substitution reactions the proton shuttle barriers (via ^{5,3}**TS**$_{PT}$) are lower in energy

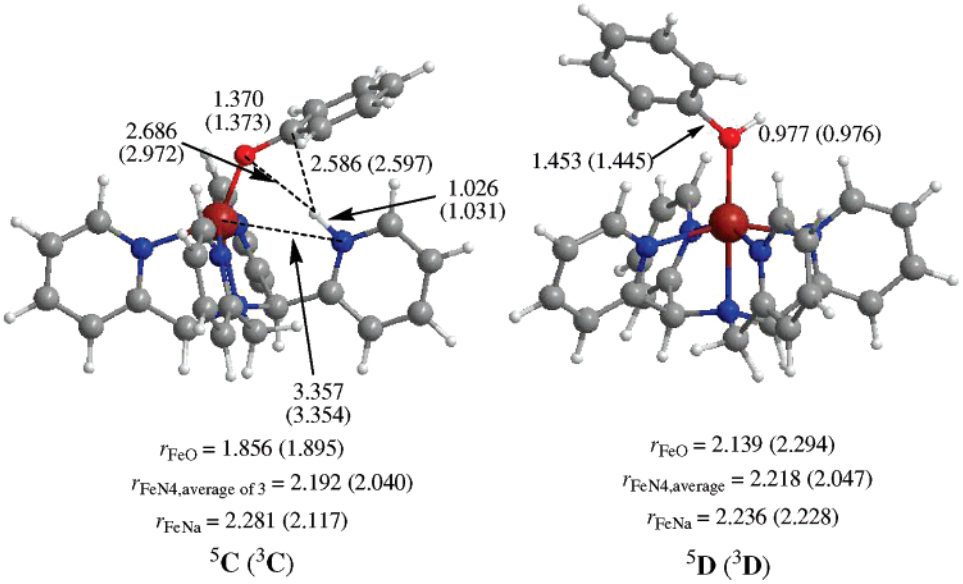

Figure 6. Optimized geometries of ^{5,3}**C** and ^{5,3}**D** with bond lengths in Å.

than the direct hydrogen transfer barriers (^{5,3}**TS**$_{HA}$), which confirms the proposed proton shuttle mechanism as the most likely reaction mechanism. In particular, the proton shuttle barrier ^{5}**TS**$_{PT,B}$ is just 0.8 kcal mol^{-1} above ^{5}**B** at the LACV3P+* level of theory (Table S3), while ZPE corrections bring it below ^{5}**B** by 0.6 kcal mol^{-1} (Figure 5). The latter artifact should be seen as an almost barrierless proton transfer from the *ipso* position in ^{5}**B** to form the proton-transfer intermediate ^{5}**C**. Moreover, the quintet pathway in Figure 5 shows barely a significant barrier for benzene hydroxylation, implying that the reaction should proceed extremely fast without accumulation of intermediates.

Finally, we ran calculations for a direct hydrogen abstraction from benzene by ^{5,3}**2** reactants to form a hydroxo−iron complex (bottom reaction in Scheme 3 above), followed by rebound of the hydroxo group to the C_6H_5• radical to form the phenol product. The two hydroxo−iron complexes (^{5,3}**E**) are local minima and are higher in energy than ^{3}**RC** by 13.9 (quintet) and 20.3 (triplet) kcal mol^{-1} at the UB3LYP/LACV3P+* level of theory with the ZPE correction included. On the triplet spin-state surface we did not manage to locate a hydrogen abstraction barrier (^{3}**TS**$_E$), which implies that ^{3}**E** is a shallow minimum, while on the quintet spin-state surface a barrier (^{5}**TS**$_E$) of 15.5 kcal mol^{-1} is obtained. The subsequent radical rebound process from ^{5,3}**E** is highly endothermic especially on the triplet spin-state surface (Figure S21). Moreover, the direct hydrogen abstraction barriers are well higher in energy than the electrophilic substitution barrier ^{5}**TS**$_B$; therefore, the hydrogen abstraction mechanism will not be able to compete with the electrophilic substitution mechanism.

So what is it that determines the relative energies of the reaction barriers, and how do external perturbations or hydrogen by deuterium substitution influence the energetics? To answer these questions, consider first in Figure 7 the geometries of the rate determining transition states (^{5,3}**TS**$_A$, ^{5,3}**TS**$_B$, and ^{5}**TS**$_E$) with bond lengths in Å and group spin densities identified. The transition states leading to the radical intermediates (^{5,3}**TS**$_B$ and ^{5}**TS**$_E$) already have significant radical character developed on the substrate moiety, whereas the ρ_{C6H6} value is low in ^{5,3}**TS**$_A$, which means that the transition states occur late. Note as well the large spin density on the N4Py unit as a result of occupation of the σ^*_{xy} orbital with one electron in the radical complexes. Due to the creation of a cationic complex in ^{5,3}**TS**$_A$ the charge distributions are quite different from those in ^{5,3}**TS**$_B$: Q_{C6H6} = 0.52 in ^{5}**TS**$_A$ and 0.23 in ^{5}**TS**$_B$, Q_{Fe} = 0.50 in ^{5}**TS**$_A$ and 0.74 in ^{5}**TS**$_B$, and Q_O = −0.25 in ^{5}**TS**$_A$ and −0.44 in ^{5}**TS**$_B$. Thus, the FeO group has a smaller positive charge in the cationic complexes as compared to the radical ones.

Subsequently, we calculated the reactants and the rate determining transition states (^{5,3}**TS**$_A$, ^{5,3}**TS**$_B$, ^{5}**TS**$_E$) in a dielectric constant of ϵ = 5.7 (Figures 5−7). Addition of a dielectric constant to the system increases all barriers and in particular the ones passing radical intermediates. Some barriers increase by more than 5 kcal mol^{-1}, but ^{5}**TS**$_A$ increases by only 2.4 kcal mol^{-1}. Nevertheless, even while ^{5}**TS**$_A$ is less destabilized than the other transition states, the ordering of the various transition states stays the same. The high barriers in an environment with a large dielectric constant may explain why experimentally the reaction between Fe=O(N4Py)$^{2+}$ and benzene did not occur. Nevertheless, our estimated free energy of activation of ^{5}**TS**$_B$ of 16.1 kcal mol^{-1} obtained at UB3LYP/LACV3P+* with ZPE, thermal, and solvent (ϵ = 5.7) corrections at the LACVP level of theory is in very good agreement with the experimental free energy of activation of 19.6 kcal mol^{-1} at 298 K (vide supra) although a different substrate was used. This is further evidence on the reliability and accuracy of the DFT/UB3LYP methodology for calculating these types of difficult reaction mechanisms.

Also shown in Figure 7 are the kinetic isotope effects (k_H/k_D, KIE) for the reaction with C_6H_6 versus C_6D_6 as calculated with the Eyring (KIE$_E$) and Wigner (KIE$_W$) models (see Methods section). Thus, the electrophilic substitution transition states give inverse kinetic isotope effects, while the

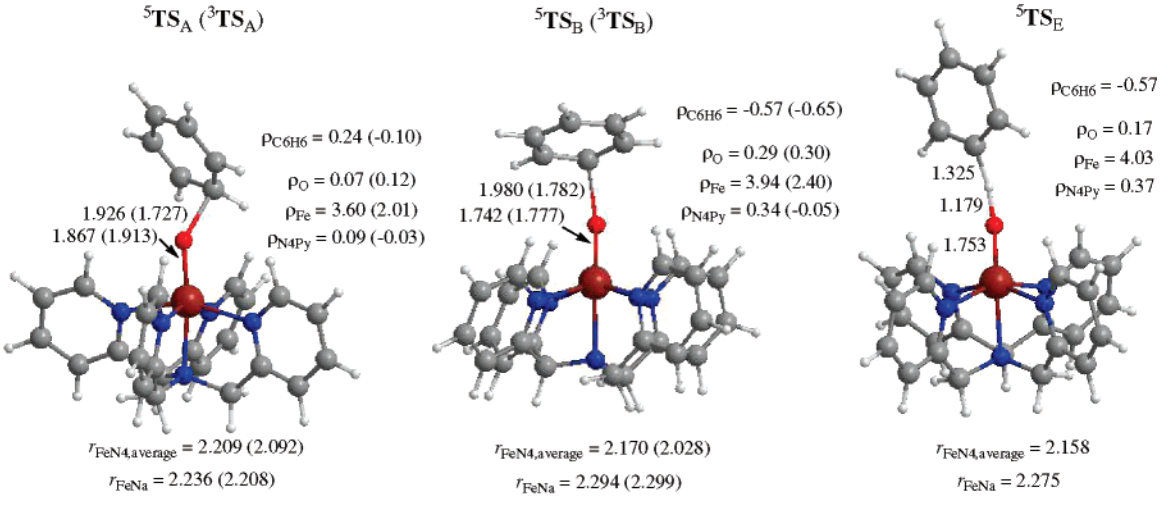

	^{5}TS$_A$ (^{3}TS$_A$)	^{5}TS$_B$ (^{3}TS$_B$)	^{5}TS$_E$
	*i*460.1 (*i*434.3)	*i*150.3 (*i*391.7)	*i*927.4
ΔG (LACV3P+*)	32.0 (38.4)	9.3 (27.4)	16.4
ΔG+E$_{\epsilon=5.7}$	29.7 (45.7)	16.1 (32.6)	21.6
KIE$_E$	0.88 (1.09)	0.86 (0.87)	10.5
KIE$_W$	0.88 (1.10)	0.86 (0.87)	13.2

Figure 7. Optimized geometries of ^{5,3}**TS**$_A$, ^{5,3}**TS**$_B$, and ^{5}**TS**$_E$ with bond lengths in Å. The imaginary frequency of the transition state is given in cm^{-1}. Also shown are group spin densities (ρ) as taken from the UB3LYP/LACV3P+* data and relative free energies (ΔG in kcal mol^{-1} relative to ^{3}**RC**) in the gas phase and under the influence of a dielectric constant of $\epsilon = 5.7$. Finally, the kinetic isotope effects of replacing C_6H_6 by C_6D_6 using the Eyring (KIE$_E$) and Wigner (KIE$_W$) models are given.

hydrogen abstraction barrier gives typical values of KIE$_E$ = 10.5 and KIE$_W$ = 13.2. Our calculated KIE values of the electrophilic substitution reactions match the experimentally obtained KIEs perfectly (compare Table 1 and Figure 7) and point to an electrophilic substitution pathway as the rate determining step in the reaction in agreement with the thermodynamics shown in Figures 4 and 5.

In summary, theory predicts that the reaction mechanism for arene hydroxylation by Fe=O(N4Py)$^{2+}$ proceeds via an electrophilic substitution reaction leading to radical intermediates and a subsequent proton-shuttle mechanism similarly to the one predicted for oxoiron heme catalysts will convert the radical intermediates into phenol. Theory predicts [Fe^{IV}-(N4Py)(O)]$^{2+}$ to react with benzene via two-state reactivity on competing triplet and quintet surfaces, whereby the quintet spin-state surface seems more reactive. However, since the reactant state is most likely to be in a dominant triplet spin state, the rate determining step in the reaction will be the spin-crossing from the triplet to the quintet spin-state surface. Thus, the spin-state crossing will involve the transfer of a β-spin electron in $\pi^*_{x^2-y^2}$ into an α-spin electron in σ^*_{xy}, and since these orbitals are located on the same center, it is expected that it will occur fast. Once the spin-state crossing has occurred and either a cationic or radical intermediate (^{5}**A** or ^{5}**B**) is formed, the reaction will proceed rapidly via a proton shuttle mechanism via one of the nitrogen atoms of the N4Py ligand that is used as a springboard to transfer the proton toward the oxygen atom. This mechanism is found to be more efficient than a direct hydrogen atom transfer.

Summary

Combined experimental and theoretical (DFT) studies into the reaction mechanism of arene hydroxylation by nonheme oxoiron complexes have been performed. Experimental evidence (e.g., KIE value of <1) demonstrates unambiguously that the reaction does not proceed via an initial hydrogen abstraction mechanism. Instead, the aromatic hydroxylation proceeds via an electrophilic substitution reaction, whereby either a radical or cationic intermediate is formed. Detailed theoretical calculations on various possible reaction mechanisms confirm the electrophilic substitution mechanism via radical intermediates as the most likely pathway. Theory has provided further insights and shown that the ligand is noninnocent and able to reshuttle the proton from the substrate via the ligand to the oxo group.

Methods

Materials and Instrumentation. Acetonitrile (anhydrous) and dichloromethane (anhydrous) were obtained from Aldrich Chemical Co. and purified by distillation over CaH_2 prior to use. All reagents purchased from Aldrich were the best available purity and used without further purification unless otherwise indicated. Iodosylbenzene was prepared by a literature method.[27] $H_2{}^{18}O$ (95% ^{18}O-enriched) was purchased from ICON Services Inc. (Summit, NJ). Fe(Bn-tpen)$(CF_3SO_3)_2$ and Fe(N4Py)$(CF_3SO_3)_2$ were synthesized according to published procedures.[28]

UV−vis spectra were recorded on a Hewlett-Packard 8453 spectrophotometer equipped with *Optostat*^{DN} variable-temperature liquid-nitrogen cryostat (Oxford Instruments). Product Analysis for the anthracene hydroxylation was performed on Agilent Technologies 6890N gas chromatography equipped with a FID detector (GC) and Thermo Finnigan Focus DSQ mass spectrometer interfaced with

(27) *Organic Syntheses*; Saltzman, H., Sharefkin, J. G., Eds.; Wiley: New York, 1973; Collect. Vol. V, p 658.
(28) (a) Duelund, L.; Hazell, R.; McKenzie, C. J.; Nielsen, L. P.; Toftlund, H. *J. Chem. Soc., Dalton Trans.* **2001**, 152−156. (b) Lubben, M.; Meetsma, A.; Wilkinson, E. C.; Feringa, B.; Que, L., Jr. *Angew. Chem., Int. Ed. Engl.* **1995**, *34*, 1512−1514.

Focus gas chromatography (GC−MS). Electrospray ionization mass spectra (ESI MS) of intermediates were collected on a Thermo Finnigan (San Jose, CA) LCQ Advantage MAX quadrupole ion trap instrument, by infusing samples directly into the source at 25 μL/min using a syringe pump. The spray voltage was set at 4.7 kV and the capillary temperature at 220 °C.

Kinetic Studies and Product Analysis. In general, [Fe(IV)(Bn-tpen)(O)]$^{2+}$ (1 mM) and [Fe(IV)(N4Py)(O)]$^{2+}$ (1 mM) were prepared by stirring Fe(Bn-tpen)$(CF_3SO_3)_2$ and Fe(N4Py)$(CF_3SO_3)_2$, respectively, with excess solid PhIO in a solvent mixture of CH_3CN and CH_2Cl_2 (1:1) at 25 °C. The reaction solutions were filtered through a 0.45-μM filter to remove solid PhIO remained. Then, appropriate amounts of anthracene (diluted in 150 μL of CH_2Cl_2) were added to the resulting solution, and spectral changes of the intermediates were directly monitored by a UV−vis spectrophotometer. Rate constants, k_{obs}, were determined by pseudo-first-order fitting of the decrease of absorption bands at 737 nm for **1** and 695 nm for **2**. All the rate constants are averages of at least three determinations.

Product analysis was performed by injecting reaction solutions directly into GC and GC−MS. Product yields were determined by comparison with standard curves of known authentic samples and decane as an internal standard. The source of oxygen in oxygenated products was determined by preparing ^{18}O-labeled [Fe(IV)(Bn-tpen)(^{18}O)]$^{2+}$ (**1**-^{18}O) and using the intermediate directly in the hydroxylation of anthracene. First, ^{18}O-labeled PhIO was prepared by treating PhIO (5 mM, diluted in 50 μL of CH_3OH) with $H_2{}^{18}O$ (10 μL, 0.52 mmol, 95% ^{18}O enriched). Then, PhI^{18}O was added to a solution of Fe(Bn-tpen)$(OTf)_2$ (1 mM) in a solvent mixture (2 mL) of CH_3CN and CH_2Cl_2 (1:1), followed by the addition of anthracene (15 mM). The resulting solution was directly analyzed by GC−MS. The ^{18}O percentage in **1**-^{18}O was determined by taking an Electrospray Ionization Mass Spectrum (Supporting Information, Figure S2).[20] To increase the accuracy of the product analysis, the hydroxylation of anthracene was performed by adding PhI^{18}O (5 mM) into a reaction solution containing Fe(Bn-tpen)$(CF_3SO_3)_2$ (1 mM) and anthracene (15 mM) under catalytic conditions in a drybox. Then, the reaction mixture was stirred for 0.5 h at room temperature. ^{16}O and ^{18}O compositions in anthraquinone were analyzed by the relative abundances of the following mass peaks: m/z = 208 (M), 210 (M + 2), and 212 (M + 4) for anthraquinone.

Theory. We have studied the reaction of Fe═O(N4Py)$^{2+}$ with benzene, by utilizing the unrestricted hybrid density functional method UB3LYP throughout.[29] Initial geometry optimizations and geometry scans to explore the potential energy surface were done with the Jaguar 5.5 program package.[30] We used a modest Los Alamos type double-ζ quality LACVP basis set on iron that contains a core potential, while all other atoms (C, N, O, H) are described with a 6-31G basis set.[31] Subsequent, single point calculations on the optimized geometries were done with the LACV3P+* basis set that contains a triple-ζ quality basis set with diffuse functions on iron (LACV3P+) and a 6-311+G* basis set on the rest of the atoms.[30] An analytical frequency calculation in Gaussian-03 confirmed the nature of the stationary points: all transition states are characterized by a single imaginary frequency for the correct mode, and all intermediates, reactants, and products have real frequencies only.[32] In the past we showed that frequencies calculated with Gaussian and Jaguar give identical results; therefore, we exported the optimized geometries from Jaguar to Gaussian for an analytical frequency analysis.[33] All energies reported in this work are energies obtained with the LACV3P+* basis set corrected with zero-point energies at LACVP level unless otherwise stated. To explore the potential energy surface, we initially ran extensive geometry scans (see the Supporting Information) between the various local minima whereby one degree of freedom was fixed. The maxima of these geometry scans were used as a starting point for the transition state calculations. To estimate the effect of the environment on the relative energies of the transition states we ran single point calculations in Jaguar using the Self-Consistent Reaction Field (SCRF) model on the rate determining transition states.[30] We used a typical dielectric constant of ϵ = 5.7 and a probe radius r = 2.67 Å mimicking chlorobenzene since this dielectric constant falls midway in the range of experimentally used solvents. Kinetic isotope effect studies for the replacement of all hydrogen atoms in benzene by deuterium atoms were studied using the semiclassical Eyring model ($KIE_E = \exp((\Delta G^{\ddagger}_D - \Delta G^{\ddagger}_H)/RT)$) and further tunneling corrections due to Wigner (KIE_W) were applied by multiplying KIE_E with the tunneling ratio ($Q_{t,H}/Q_{t,D}$) whereby $Q_t = 1 + (h\nu/kT)^2/24$. In these equations $\Delta G^{\ddagger}$ is the free energy of activation, R is the gas constant, T is the temperature (298 K), h is Planck's constant, k is Boltzmann's constant, and ν is the imaginary frequency in the transition state.[34]

Acknowledgment. This research was supported by the Creative Research Initiative Program of MOST/KOSEF (W.N.), the BK 21 Program (K.O. and A.-R.H.), and the National Service of Computational Chemistry Software (NSCCS) for providing valuable CPU time (S.P.dV.). We thank Dr. Mi Sook Seo at Ewha Womans University for taking ESI MS of intermediates.

Supporting Information Available: Experimentally obtained UV−vis spectral changes of **2** (Figure S1), the mass spectrum of **1**-^{18}O (Figure S2), tables of first-order rate constants of various *para*-X-substituted anthracenes by **1** (Table S1**)**, absolute and relative energies, group spin densities, charges of all optimized geometries using either the LACVP or LACV3P+* basis set, and kinetic isotope effects, five figures with geometry scans and 15 figures with optimized geometries and Cartesian coordinates of all species mentioned in this work, and ref 32 in full.

IC700462H

(29) (a) Becke, A. D. *J. Chem. Phys*. **1993**, *98*, 5648−5652. (b) Lee, C.; Yang, W.; Parr, R. G. *Phys. Rev. B* **1988**, *37*, 785−789.
(30) Jaguar 5.5; Schrödinger, LLC: Portland, OR, 2003.
(31) Hay, P. J.; Wadt, W. R. *J. Chem. Phys*. **1985**, *82*, 299−310.
(32) Frisch, M. J. et al. *Gaussian-03: Revision C.01*; see the Supporting Information for the complete reference citation.
(33) Ogliaro, F.; Harris, N.; Cohen, S.; Filatov, M.; de Visser, S. P.; Shaik, S. *J. Am. Chem. Soc*. **2000**, *122*, 8977−8989.
(34) (a) Kumar, D.; de Visser, S. P.; Sharma, P. K.; Cohen, S.; Shaik, S. *J. Am. Chem. Soc*. **2004**, *126*, 1907−1920. (b) de Visser, S. P. *J. Biol. Inorg. Chem*. **2006**, *11*, 168−178.